Emergent electromagnetic induction in a helical-spin magnet

https://doi.org/10.1038/s41586-020-2775-x

Received: 20 June 2020

Accepted: 4 August 2020

Published online: 7 October 2020

Check for updates

Tomoyuki Yokouchi[1]✉, Fumitaka Kagawa[1,2], Max Hirschberger[1,3], Yoshichika Otani[1,4], Naoto Nagaosa[1,2] & Yoshinori Tokura[1,2,5]✉

An inductor, one of the most fundamental circuit elements in modern electronic devices, generates a voltage proportional to the time derivative of the input current[1]. Conventional inductors typically consist of a helical coil and induce a voltage as a counteraction to time-varying magnetic flux penetrating the coil, following Faraday's law of electromagnetic induction. The magnitude of this conventional inductance is proportional to the volume of the inductor's coil, which hinders the miniaturization of inductors[2]. Here, we demonstrate an inductance of quantum-mechanical origin[3], generated by the emergent electric field induced by current-driven dynamics of spin helices in a magnet. In microscale rectangular magnetic devices with nanoscale spin helices, we observe a typical inductance as large as ~400 nanohenry, comparable in magnitude to that of a commercial inductor, but in a volume about a million times smaller. The observed inductance is enhanced by nonlinearity in current and shows non-monotonous frequency dependence, both of which result from the current-driven dynamics of the spin-helix structures. The magnitude of the inductance rapidly increases with decreasing device cross-section, in contrast to conventional inductors. Our findings may pave the way to microscale, simple-shaped inductors based on emergent electromagnetism related to the quantum-mechanical Berry phase.

Inductors are ubiquitous in contemporary electronics, used in analogue circuits and information processing, in transformers, filters and resonators, to name but a few applications. Conventional inductors or induction coils based on classical electromagnetism store the magnetic energy $LI^2/2$ (where L is inductance and I is input current) and generate a voltage proportional to $\mathrm{d}I/\mathrm{d}t$. As the magnitude of the inductance is proportional to the product of the coil's winding number and its cross-section, it is difficult to reduce the dimensions of the device while keeping L large enough. In superconductors, another inductance mechanism, known as kinetic inductance, offers inductance inversely proportional to the cross-section[4]. However, using superconductors in electric devices is still challenging, and available current densities are limited by the critical current density for the superconducting ground state. Thus, a new principle for inductors is highly desirable.

Our approach to developing microscale inductors that overcome these issues is based on the use of current-induced spin dynamics in a helical-spin magnet. When conduction electrons flow with their spin direction aligned along an underlying spin structure, they can acquire a Berry phase[5,6]. This acts as an effective electromagnetic field, termed the emergent electromagnetic field. In the continuum limit, the emergent magnetic (b_i) and electric (e_i) fields are described as[6,7]

$$b_i = \frac{h}{8\pi e}\epsilon_{ijk}\mathbf{n}\cdot(\partial_j\mathbf{n}\times\partial_k\mathbf{n}) \quad (1)$$

$$e_i = \frac{h}{2\pi e}\mathbf{n}\cdot(\partial_i\mathbf{n}\times\partial_t\mathbf{n}), \quad (2)$$

where $\mathbf{n}$ is a unit vector parallel to the direction of spins, ϵ_{ijk} is the Levi–Civita symbol, and the Einstein convention is adopted. The emergent magnetic field arises from non-coplanar spin structures and is proportional to the solid angle subtended by $\mathbf{n}$. One example of b_i is found in topological spin structures called skyrmions[7–9], in which the direction of spins wraps the unit sphere exactly once (Fig. 1a). Hence, skyrmions carry emergent magnetic field, which leads to the topological Hall effect[10]. In contrast, non-collinear spin structures such as helices and ferromagnetic domain walls cannot produce b_i because the solid angle covered by $\mathbf{n}$ is zero (Fig. 1b).

As opposed to b_i, however, e_i is related to the dynamics of spin structures and proportional to the solid angle swept out by $\mathbf{n}(t)$. Hence, the motion of non-collinear spin structures can induce e_i, also called spin-motive force[11–17]. Motion of the non-collinear spin structures can be generally described by two collective coordinates[3,13,18]: the position X and the angle ϕ representing a tilt of the spin from the helical plane (see Fig. 1c for the definition). Because X and ϕ are canonically conjugate to each other, a change in position X always accompanies the tilt of spins from the helical plane (that is, a change in ϕ). Consequently, when the non-collinear spin structures are on the move, the solid angle swept by $\mathbf{n}(t)$ is non-zero (Fig. 1c), and an emergent electric field e_i

[1]RIKEN Center for Emergent Matter Science (CEMS), Wako, Japan. [2]Department of Applied Physics, The University of Tokyo, Tokyo, Japan. [3]Quantum-Phase Electronics Center (QPEC), The University of Tokyo, Tokyo, Japan. [4]Institute for Solid State Physics (ISSP), The University of Tokyo, Kashiwa, Japan. [5]Tokyo College, The University of Tokyo, Tokyo, Japan. ✉e-mail: tomoyuki.yokouchi@riken.jp; tokura@riken.jp

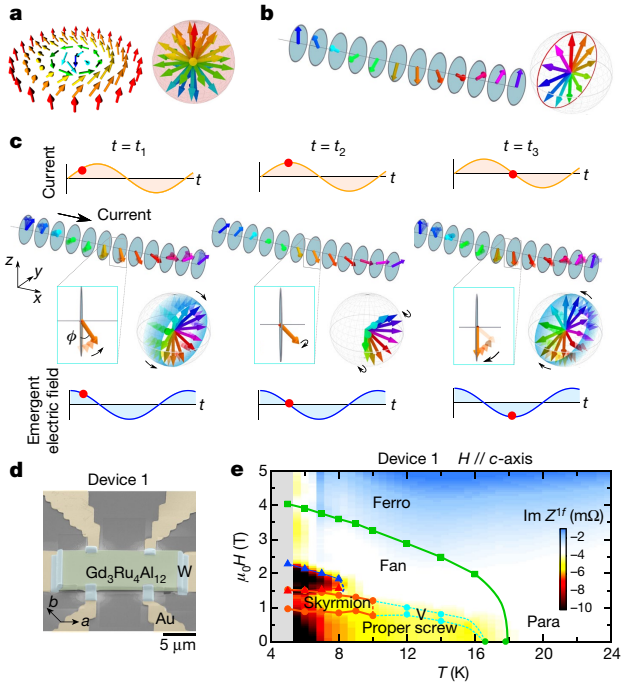

Fig. 1 | Concept of emergent inductance. a, **b**, Schematics for spin configurations of a skyrmion (**a**) and a proper-screw helix (**b**) in real space (left) and its projection into the unit sphere (right). **c**, Schematics for spin configurations under the current-driven motion of a proper-screw helix in real space and its projection into the unit sphere at several points in time. The light blue shading in the unit spheres shows the solid angle swept by the direction of the spins. The magnitudes of current and emergent electric field at the corresponding time points are denoted by the red points in the top and bottom panels, respectively. **d**, Scanning electron microscope image of a thin-plate $Gd_3Ru_4Al_{12}$ device, approximately 300 nm thick and 5 μm wide. **e**, Contour mapping of the imaginary part of the complex impedance ($\mathrm{Im}\,Z^{1f}$) measured with $j_0 = 3.3 \times 10^8$ A m^{-2} and $f = 10$ kHz. Fan, fan structure region; Ferro, ferromagnetic region; para, paramagnetic region. Different symbols indicate different phase boundaries.

proportional to the time-derivative of ϕ, $\partial_t\phi$, is generated[3,13]. For example, in the case of a proper-screw helix, the emergent electric field e_x can be described as[3]:

$$e_x = \frac{Ph}{e\lambda}\partial_t\phi, \tag{3}$$

where λ is the period of the helix, P is spin polarization factor, e is the charge on the electron, and the x-axis is taken parallel to the magnetic modulation vector Q (see Supplementary Information for details). Because the canonical conjugate relation between X and ϕ holds regardless of the direction of the helical plane[18], e_x can also be generated in cycloidal-type spin modulations. So far, emergent electric fields arising from the motion of ferromagnetic domain walls driven by magnetic field (H) have been reported experimentally[14–16]. We note that the emergent electric field is also derived from generalized Faraday's law[13].

In the case of current-driven motion of non-collinear spin structures, the emergent electric field is predicted to produce an inductive voltage[3]. When a non-collinear spin structure is driven by a current parallel to Q due to spin-transfer torque or spin–orbit torque (Fig. 1c), ϕ can be phenomenologically described as $\phi = Aj_x + Bj_x^3 + Cj_x^5 + \cdots$, where j_x is the current density. Since e_i due to the motion of non-collinear structures is proportional to $\partial_t\phi$ as described above, the consequent e_i is proportional to the time derivative of the current density ($\partial_t j_x$). In other words, the emergent electric field generated by current-driven motion produces an inductive voltage. Hereafter, we call this inductance 'emergent inductance'. The emergent inductive voltage can be described as

$$\begin{aligned} V &= e_x d_{\mathrm{electrode}} \\ &\propto (\partial_t\phi) d_{\mathrm{electrode}} \\ &= d_{\mathrm{electrode}}(A + 3Bj_x^2 + 5Cj_x^4 + \cdots)\frac{\mathrm{d}j_x}{\mathrm{d}t} \\ &= \frac{d_{\mathrm{electrode}}}{S_c}\left(A + 3B\frac{I^2}{S_c^2} + 5C\frac{I^4}{S_c^4} + \cdots\right)\frac{\mathrm{d}I}{\mathrm{d}t}, \end{aligned} \tag{4}$$

where $d_{\mathrm{electrode}}$ and S_c are the distance of electrodes and the cross-sectional area of the device, respectively (see Supplementary Information for details). Notably, since the current density is inversely proportional to S_c, the emergent inductance increases with decreasing S_c under fixed input current. In particular, the higher-order terms arising from the nonlinearity of ϕ make this increase more steeply than the inverse of S_c, and as will be discussed below, the contribution from higher-order terms is dominant.

To experimentally investigate the emergent inductance, we focus on the short-period helimagnet $Gd_3Ru_4Al_{12}$, in which various non-collinear spin structures such as proper-screw, magnetic skyrmion and transverse conical (TC), with helical pitch $\lambda \approx 2.8$ nm, appear owing to competition among the Ruderman–Kittel–Kasuya–Yosida (RKKY) interaction, magnetic anisotropy and thermal fluctuations[19–23]. The short helical pitch and weak magnetic anisotropy of $Gd_3Ru_4Al_{12}$ provide an ideal platform for exploration of the emergent inductance because the emergent inductance is inversely proportional to λ (equation (3)) and spins move easily owing to weak magnetic anisotropy. By using the focused ion beam (FIB) technique, we fabricated microscale rectangular thin-plate devices of $Gd_3Ru_4Al_{12}$ (Fig. 1d; see Methods and Extended Data Figs. 1 and 2 for the determination of magnetic phases for the thin-plate devices). First, we investigate the emergent inductance by using a standard lock-in technique, in which the inductance appears in the imaginary part of the complex impedance ($\mathrm{Im}\,Z^{1f}$), which is also called reactance (see Methods). Here, $1f$ represents the fundamental frequency components in the lock-in measurement.

Figure 2a–d presents H-dependent $\mathrm{Im}\,Z^{1f}$ measured with current-density amplitude $j_0 = 3.3 \times 10^8$ A m^{-2}, frequency $f = 10$ kHz and H // c-axis. Prominent signals of $\mathrm{Im}\,Z^{1f}$ are observed in the proper-screw and TC phases. In contrast, in ferromagnetic and paramagnetic phases, $\mathrm{Im}\,Z^{1f}$ is as small as −4 mΩ, which we assign to background signal, probably from contact electrodes and cables connecting the sample and the lock-in amplifier. The correspondence between enhanced $\mathrm{Im}\,Z^{1f}$ signals and the non-collinear phases is further confirmed from the contour map of $\mathrm{Im}\,Z^{1f}$ in the temperature (T)–H phase diagram (Fig. 1e). As presented in Extended Data Fig. 3, the imaginary part of background-subtracted complex impedance ($\mathrm{Im}\,\Delta Z^{1f}$) is linearly proportional to the frequency from 0 kHz to10 kHz, which indicates that $\mathrm{Im}\,\Delta Z^{1f}$ is governed by the inductive reactance, that is, $\mathrm{Im}\,\Delta Z^{1f} = 2\pi f L'$ (see also Methods; frequency dependence above 10 kHz is discussed later).

By fabricating more than ten devices of different lengths, thicknesses and widths, we confirmed reproducibility and excluded the possibility that the observed $\mathrm{Im}\,Z^{1f}$ signal was due to non-intrinsic effects such as external contact contributions (see Methods and Extended Data Fig. 4). We note that the range of the magnitude of j_0 used in this study is much smaller than the typical critical current density for the translational motion of helices[24]. Hence, the relaxation-type motion[25] probably occurs because of spin-transfer torque in the present case (see also Methods).

As shown in Fig. 2a–c, $\mathrm{Im}\,Z^{1f}$ in the fan phase is much smaller than that in the proper-screw and TC phases, although the fan structure is also non-collinear. This is well explained by the emergent inductance mechanism; as shown in Fig. 2e–j, the direction of spins of the

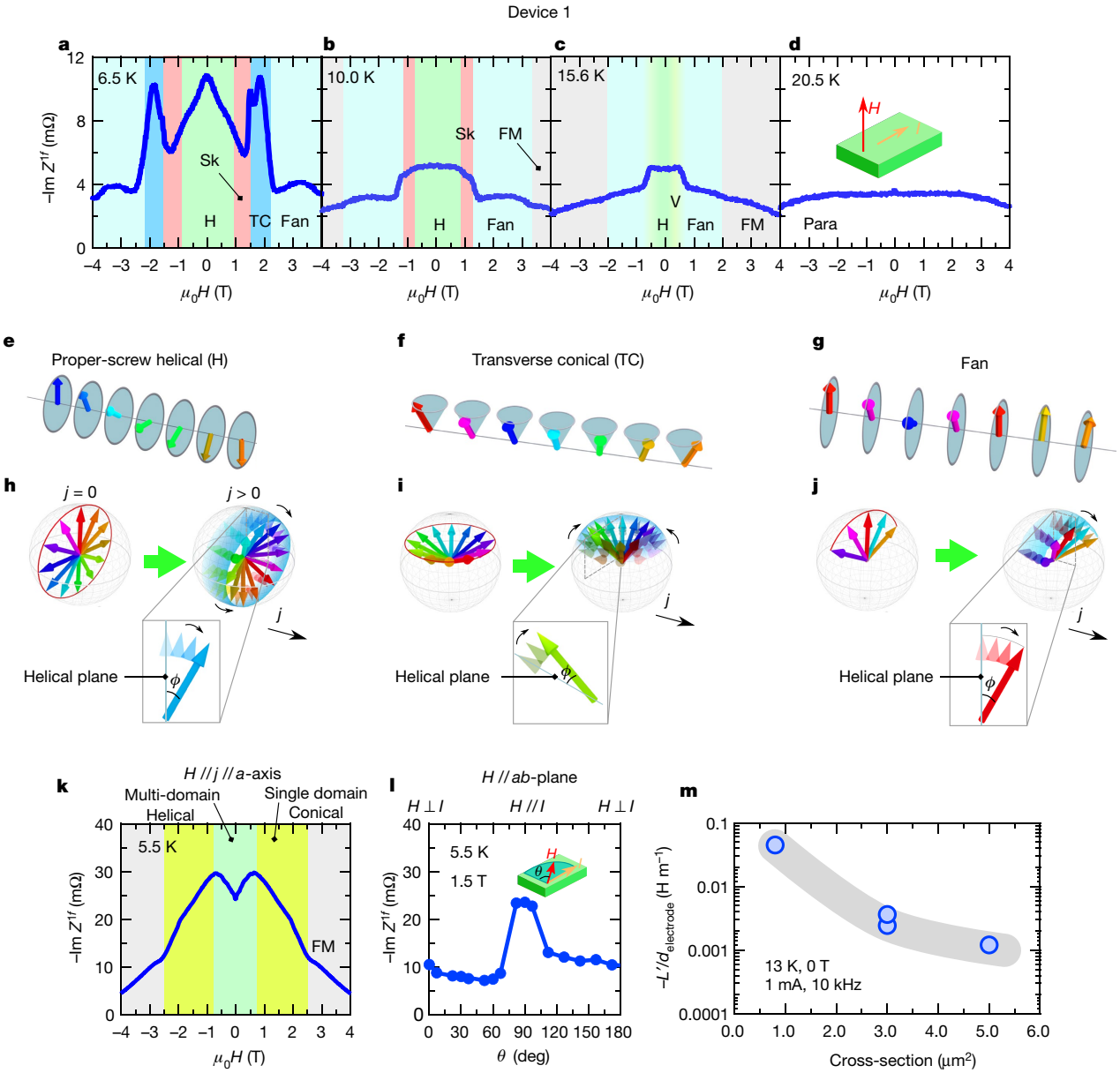

Fig. 2 | Emergent inductance in $Gd_3Ru_4Al_{12}$. a–d, Magnetic field dependence of the imaginary part of the complex impedance ($Im\,Z^{1f}$) measured with $j_0 = 3.3 \times 10^8$ A m^{-2}, $f = 10$ kHz and $H // c$-axis at various temperatures. The green, pink, blue, light blue and grey shading represents proper-screw helical (H), skyrmion (Sk), TC, fan and induced ferromagnetic (FM) phases, respectively. **e–g**, Schematics for spin configurations of proper-screw helical (**e**), TC (**f**) and fan (**g**) structures in real space. **h–j**, Schematics for current-induced motion for proper-screw helical (**h**), TC (**i**) and fan (**j**) structures projected onto the unit sphere. **k**, H-dependence of $Im\,Z^{1f}$ measured with $j_0 = 3.3 \times 10^8$ A m^{-2}, $f = 10$ kHz and $H // j // a$-axis. **l**, Angle (θ) dependence of $Im\,Z^{1f}$ in the single-domain conical phase measured with $j_0 = 3.3 \times 10^8$ A m^{-2} and $f = 10$ kHz. Here, H is rotated in the ab-plane as shown in the inset. **m**, Magnitude of the inductance (L') normalized by the electrode distance ($d_{electrode}$) as a function of the cross-section of the devices. The thick grey line is a guide to the eye.

fan structure does not rotate by 2π, in contrast to the screw and TC structure (red lines in Fig. 2h–j). Hence, when the fan structure is driven by current, the solid angle swept by $\mathbf{n}(t)$ (light blue region in Fig. 2h–j) is smaller than those for the screw and TC structures, which leads to the smaller emergent electric field. Although current-driven motion of skyrmions also generates the emergent electric field[7,26,27], it does not contribute to $Im\,Z^{1f}$ in the present set-up. This is because the emergent electric field due to skyrmion motion is generated perpendicular to the current direction[7,26,27]. Thus, the small $Im\,Z^{1f}$ signal observed in the skyrmion phase perhaps arises from coexisting proper-screw and TC phases. Phase coexistence is indicated by the topological Hall signal associated with the skyrmion phase (see Methods).

According to equation (3), the emergent electric field is expected to be generated parallel to Q. Hence, to further confirm that the observed $Im\,Z^{1f}$ signals stem from the emergent inductance, we investigate its dependence on Q-direction, which is controlled with H applied in the ab-plane (see Methods and Extended Data Fig. 5). Figure 2k presents the H dependence of $Im\,Z^{1f}$ measured with $H // I // a$-axis where I is current. The magnitude of $Im\,Z^{1f}$ reaches its maximum when the multi-domain Q state is transformed to the single-Q (longitudinal) conical state with $Q // H // I$. Additionally, as shown in Fig. 2l, when H is rotated within the ab-plane in the single-Q conical state, $Im\,Z^{1f}$ is greatest at $Q // I$ ($\theta = 90°$). These results indicate that the inductive voltage is generated parallel to the Q direction, in accordance with the expected behaviour of the emergent inductance. The reduction of $Im\,Z^{1f}$ with increasing H in the single-Q

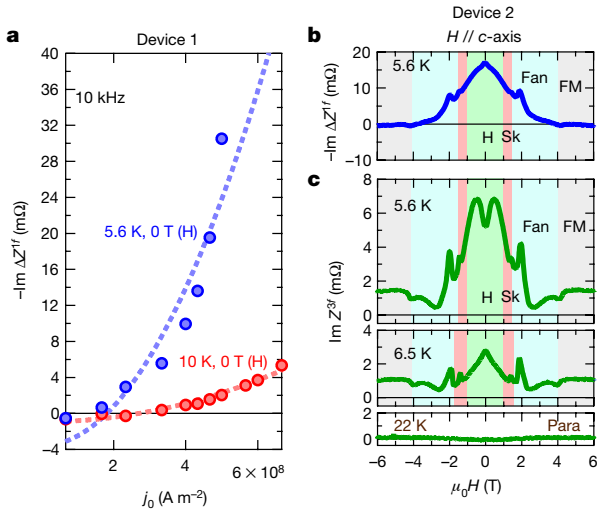

Fig. 3 | Nonlinearity of emergent inductance. a, Current-density dependence of the imaginary part of the background-subtracted complex impedance. The dashed lines are fits to theory. **b**, **c**, The magnetic field dependence of $\mathrm{Im}\,\Delta Z^{1f}$ (**b**) and the imaginary part of the third-harmonic complex impedance ($\mathrm{Im}\,Z^{3f}$) (**c**) measured with $j_0 = 3.3 \times 10^8$ A m^{-2} and $f = 10$ kHz. The green, pink, light blue and grey shading represents H, Sk, fan and induced FM phases, respectively, as in Fig. 2.

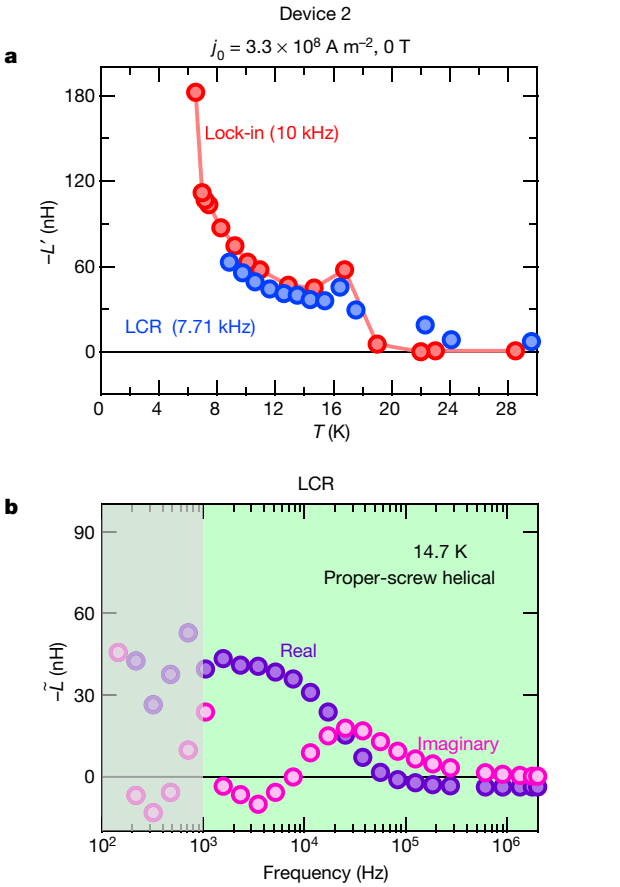

Fig. 4 | Frequency dependence of emergent inductance. a, Temperature dependence of the real part of complex inductance L' measured with a lock-in amplifier (red) and an LCR meter (blue). **b**, Frequency dependence of the complex inductance ($\tilde{L}$) measured with the LCR meter. In the low-frequency region, the impedance ($\tilde{Z}(\omega)$) was proportional to the frequency, and especially below 1 kHz, $\tilde{Z}(\omega)$ was smaller than the background noise (see Extended Data Fig. 6a). Thus we discarded $\tilde{L}$ calculated from the corresponding $\tilde{Z}(\omega)$ (grey-shaded region).

conical state (Fig. 2k) is also consistent with the emergent inductance mechanism; the cone-angle of the conical structure decreases with increasing H, which reduces the solid angle swept by $\mathbf{n}(t)$ and thus e_x.

We estimate the magnitude of the emergent inductance (L') by using the relationship $\mathrm{Im}\,\Delta Z^{1f} = 2\pi f L'$. At $\mu_0 H = 0$ T, $T = 6.5$ K, $j_0 = 3.3 \times 10^8$ A m^{-2} and $f = 10$ kHz (Fig. 2a), for example, L' is approximately −100 nH. In contrast to conventional inductors, the magnitude of L' increases when decreasing the cross-section of the thin plate, as expected in the emergent inductance formalism (Fig. 2m). The sign of the observed inductance is negative, unlike conventional inductors; conventional inductance is related to the magnetic energy[1], and hence negative inductance is energetically unstable. Because the emergent inductance mechanism is different, the magnetic energy is irrelevant in the present case, and the negative sign is also allowed. Incidentally, negative inductance can be used for applications: for example, high-speed circuits and chaotic oscillators are proposed[28]. Furthermore, positive emergent inductance can also be realized (see Supplementary Information for detailed discussion).

The inductance shows current-nonlinear behaviour, which further supports the notion that the observed inductance arises from the emergent electric field induced by current-driven motion of helical spin structures. As shown in Fig. 3a, $\mathrm{Im}\,\Delta Z^{1f}$ strongly depends on the current density. This is not due to the heating effect (see Methods). Since the emergent electric field is proportional to $\partial_t \phi$, the observed nonlinearity of $\mathrm{Im}\,\Delta Z^{1f}$ is attributed to the nonlinearity of ϕ with respect to j. In fact, the equations of motion for the non-collinear spin structures possess nonlinear terms[3,18]. If we phenomenologically describe ϕ up to the third order of j as $\phi = Aj + Bj^3$, $\mathrm{Im}\,\Delta Z^{1f}$ in the proper-screw state is given by $\mathrm{Im}\,\Delta Z^{1f} = \frac{\hbar\omega d}{e\lambda S_c}\left(A + \frac{3}{4}B j_0^2\right)$ (see Supplementary Information). The observed j-dependence is fitted well by this equation (dashed lines in Fig. 3a). The nonlinear behaviour is also confirmed from higher-harmonic measurement; as presented in Fig. 3b, c, the imaginary part of the third-harmonic complex impedance ($\mathrm{Im}\,Z^{3f}$) is enhanced in the non-collinear phases and disappears above the transition temperature. The magnitudes of $\mathrm{Im}\,\Delta Z^{1f}$ and $\mathrm{Im}\,Z^{3f}$ are consistent with each other (see Supplementary Information for details).

Finally, we discuss the frequency dependence of the emergent inductance in the high-frequency region. As mentioned above, we performed measurements with the lock-in amplifier below 10 kHz. To investigate the frequency dependence in the range of much higher frequencies, we measured the complex impedance with an LCR meter and analysed the data by assuming a frequency-dependent complex inductance, $\tilde{L}(\omega) = L'(\omega) + iL''(\omega)$ (see Methods). Below 10 kHz, $\tilde{L}(\omega)$ measured by the LCR meter is almost the same as that measured with the lock-in amplifier (Fig. 4a and Extended Data Fig. 6); L'' is almost negligible and frequency-independent, whereas L' is observed in the non-collinear phases. Above 10 kHz, in contrast, L' shows a rapid decrease concomitant with a peak of L'' (Fig. 4b). This Debye-type relaxation originates from the frequency dependence of current-driven motion of the spin structures determined by the extrinsic pinning, for example, due to impurities; the spins cannot fully follow alternating currents with a frequency above 10 kHz, resulting in smaller amplitude of ϕ and thus L' (see Supplementary Information for detailed discussion).

We have demonstrated a mechanism to generate electromagnetic inductance originating from the emergent electric field. Here, the quantum-mechanical Berry phase due to the current-driven motion of short-pitch helical spin structures plays an important part. The emergent inductance provides an opportunity for miniaturization of an inductor without reducing the magnitude of the inductance and without the need for manufacturing complex microstructures[3]. To realize emergent inductance at room temperature, non-collinear spin structures due to the Dzyaloshinskii–Moriya interaction are also promising candidates[29,30]. Additionally, control of magnetic anisotropy by

voltage can be used for tuning the current-induced dynamics of a helix and thus the magnitude of inductance.

Online content

Any methods, additional references, Nature Research reporting summaries, source data, extended data, supplementary information, acknowledgements, peer review information; details of author contributions and competing interests; and statements of data and code availability are available at https://doi.org/10.1038/s41586-020-2775-x.

1. Landau, L. D. & Lifshitz, E. M. *Electrodynamics of Continuous Media* Ch. 32 (Pergamon, 1960).
2. Kang, J. et al. On-chip intercalated-graphene inductors for next-generation radio frequency electronics. *Nat. Electron*. **1**, 46–51 (2018).
3. Nagaosa, N. Emergent inductor by spiral magnets. *Jpn J. Appl. Phys*. **58**, 120909 (2019).
4. Meservey, R. & Tedrow, P. M. Measurements of the kinetic inductance of superconducting linear structures. *J. Appl. Phys*. **40**, 2028 (1969).
5. Berry, M. V. Quantal phase factors accompanying adiabatic changes. *Proc. R. Soc. Lond. A* **392**, 45–57 (1984).
6. Xiao, D., Chang, M.-C. & Niu, Q. Berry phase effects on electronic properties. *Rev. Mod. Phys*. **82**, 1959–2007 (2010).
7. Nagaosa, N. & Tokura, Y. Topological properties and dynamics of magnetic skyrmions. *Nat. Nanotechnol*. **8**, 899–911 (2013).
8. Mühlbauer, S. et al. Skyrmion lattice in a chiral magnet. *Science* **323**, 915–919 (2009).
9. Yu, X. Z. et al. Real-space observation of a two-dimensional skyrmion crystal. *Nature* **465**, 901–904 (2010).
10. Neubauer, A. et al. Topological Hall effect in the A phase of MnSi. *Phys. Rev. Lett*. **102**, 186602 (2009).
11. Volovik, G. E. Linear momentum in ferromagnets. *J. Phys. C* **20**, L83 (1987).
12. Froelich, J. & Studer, U. M. Gauge invariance and current algebra in nonrelativistic many-body theory. *Rev. Mod. Phys*. **65**, 733–802 (1993).
13. Barnes, S. E. & Maekawa, S. Generalization of Faraday's law to include nonconservative spin forces. *Phys. Rev. Lett*. **98**, 246601 (2007).
14. Yang, S. A. et al. Universal electromotive force induced by domain wall motion. *Phys. Rev. Lett*. **102**, 067201 (2009).
15. Hayashi, M. et al. Time-domain observation of the spinmotive force in permalloy nanowires. *Phys. Rev. Lett*. **108**, 147202 (2012).
16. Yamane, Y. et al. Continuous generation of spinmotive force in a patterned ferromagnetic film. *Phys. Rev. Lett*. **107**, 236602 (2011).
17. Yamane, Y., Ieda, J. & Sinova, J. Electric voltage generation by antiferromagnetic dynamics. *Phys. Rev. B* **93**, 180408 (2016).
18. Tatara, G. & Kohno, H. Theory of current-driven domain wall motion: spin transfer versus momentum transfer. *Phys. Rev. Lett*. **92**, 086601 (2004).
19. Gladyshevskii, R. E., Strusievicz, O. R., Cenzual, K. & Parthé, E. Structure of $Gd_3Ru_4Al_{12}$, a new member of the $EuMg_{5.2}$ structure family with minority atom clusters. *Acta Crystallogr. B* **49**, 474–478 (1993).
20. Niermann, J. & Jeitschko, W. Ternary rare earth (R) transition metal aluminides $R_3T_4Al_{12}$ (T = Ru and Os) with $Gd_3Ru_4Al_{12}$ type structure. *Z. Inorg. Gen. Chem*. **628**, 2549 (2002).
21. Nakamura, S. et al. Spin trimer formation in the metallic compound $Gd_3Ru_4Al_{12}$ with a distorted kagome lattice structure. *Phys. Rev. B* **98**, 054410 (2018).
22. Chandragiri, V., Iyer, K. K. & Sampathkumaran, E. V. Magnetic behavior of $Gd_3Ru_4Al_{12}$, a layered compound with distorted kagomé net. *J. Phys. Condens. Matter* **28**, 286002 (2016).
23. Hirschberger, M. et al. Skyrmion phase and competing magnetic orders on a breathing kagomé lattice. *Nat. Commun*. **10**, 5831 (2019).
24. Iwasaki, J., Mochizuki, M. & Nagaosa, N. Universal current–velocity relation of skyrmion motion in chiral magnets. *Nat. Commun*. **4**, 1463 (2013).
25. Kleemann, W. Universal domain wall dynamics in disordered ferroic materials. *Annu. Rev. Mater. Res*. **37**, 415 (2007).
26. Schulz, T. et al. Emergent electrodynamics of skyrmions in a chiral magnet. *Nat. Phys*. **8**, 301–304 (2012).
27. Yokouchi, T. et al. Current-induced dynamics of skyrmion strings. *Sci. Adv*. **4**, eaat1115 (2018).
28. Funato, H., Kawamura, A. & Kamiyama, K. Realization of negative inductance using variable active–passive reactance (VAPAR). *IEEE Trans. Power Electron*. **12**, 589 (1997).
29. Zhang, S. L. et al. Room-temperature helimagnetism in FeGe thin films. *Sci. Rep*. **7**, 123 (2017).
30. Emori, S., Bauer, U., Ahn, S.-M., Martinez, E. & Beach, G. S. D. Current-driven dynamics of chiral ferromagnetic domain walls. *Nat. Mater*. **12**, 611–616 (2013).

Methods

Device fabrication

Using the FIB technique (NB-5000, Hitachi), we cut thin plates out of a single crystal of $Gd_3Ru_4Al_{12}$. The single crystals were grown under argon gas flow with a floating zone furnace equipped for high-vacuum operation. Our thin plates were mounted on a silicon stage and were fixed by FIB-assisted tungsten deposition. We used electron-beam gold deposition or FIB-assisted tungsten deposition to make electrical contact to the sample.

Transport measurement

Complex impedance was measured by the lock-in technique (SR-830, Stanford Research Systems, and LI5640, NF Corporation) and the LCR meter (Agilent Technologies, E4980A). In the lock-in measurement, we input a sine-wave current ($I = I_0 \sin \omega t$) and recorded both in-phase (V_X^{1f}) and out-of-phase (V_Y^{1f}) voltage components with a standard four-terminal method. The imaginary part of the linear impedance, namely the reactance, is defined as $\mathrm{Im}Z^{1f} = V_Y^{1f}/I$. For the estimation of the inductance, we assumed that Im Z^{1f} was governed by the inductive reactance. In addition, since the lock-in measurement was performed below 10 kHz, we ignored the frequency dependence and the imaginary part of the inductance, both of which become important only above 10 kHz, as revealed by LCR measurement. Hence, the real part of the inductance can be described as $L' = \mathrm{Im}\,\Delta Z^{1f}/\omega$, where $\omega = 2\pi f$ is the angular frequency and Im ΔZ^{1f} is the imaginary part of background-subtracted complex impedance. Here, we ascribed Im Z^{1f} observed in the paramagnetic phase to the background contribution. For the third-harmonic measurement, we measured the out-of-phase third-harmonic voltage component (V_Y^{3f}) and defined the third harmonic imaginary part of impedance (Im Z^{3f}) as $\mathrm{Im}Z^{3f} = V_Y^{3f}/I$; in this case, the background contribution was negligibly small, which indicates that the background signal is caused by linear reactance probably resulting from contact electrodes and cables connecting the sample and the lock-in amplifier.

In measurements with the LCR meter, we used a two-terminal method and corrected the contribution from the cables with a standard open/short/load correction procedure. To remove the contribution from the contacts and extract the bulk contribution of the complex impedance $\bar{Z}(\omega)$, we subtracted the contact contribution that was estimated above the transition temperature from the measured data. To estimate the inductance, we assume a series connection of a frequency-independent resistance (R) and a frequency-dependent complex inductance $\tilde{L}(\omega) = L'(\omega) + iL''(\omega)$. Under this assumption, the relationship among $\bar{Z}(\omega)$, $\tilde{L}(\omega)$ and R is described as $\bar{Z}(\omega) = \tilde{L}(\omega) + R$. Then $L'(\omega)$ and $L''(\omega)$ are calculated from the experimentally obtained value of $\bar{Z}(\omega)$ as follows: $L'(\omega) = \mathrm{Im}\,\bar{Z}(\omega)/\omega$ and $L''(\omega) = [\mathrm{Re}\,\bar{Z}(\omega) - R]/\omega = [\mathrm{Re}\,\bar{Z}(\omega) - \mathrm{Re}\,\bar{Z}(0)]/\omega$.

Considering the increase in sample temperature owing to Joule heating, we derived the sample temperature from the longitudinal resistivity of the sample itself for all measurements. In the measurement of the current-density dependence, we kept the sample temperature constant by adjusting the temperature of the heat bath. In addition, even if a possible temperature gradient originating from Joule heating generates pure spin current due to the spin Seebeck effect, this does not contribute to Im Z^{1f}: since the present device is a symmetric single layer, the pure spin current is not converted to a voltage signal, which generally requires asymmetric structure.

The type of motion of spin structures

On the basis of the current density and frequency dependencies of the inductance signals, we conclude that the relaxation dynamics of the helix due to spin-transfer torque results in the observed inductance signals in the present study.

The amplitude of the alternating current density used in this study (~10^8 A m^{-2}) is much smaller than the critical current density for translational motion (~10^{11} A m^{-2}). Generally, in such cases, relaxation dynamics is known to occur[25]. Hence, we conclude that the motion of helices shows relaxation dynamics in which the position of the helical spin structure oscillates at the local minimum of the free energy.

The observed frequency profile is also consistent with relaxation dynamics. As shown in Fig. 4, we observed a Debye-type frequency profile with characteristic frequency of approximately 10 kHz. Relaxation dynamics usually shows a Debye-type frequency profile whose characteristic frequency is of the order of kilohertz, consistent with our observations.

Resistivity and transition temperatures for $Gd_3Ru_4Al_{12}$ thin-plate sample

Extended Data Fig. 1a shows the temperature (T) dependence of the longitudinal resistivity (ρ_{xx}) in a thin-plate device of $Gd_3Ru_4Al_{12}$. The temperature dependence of the thin-plate sample is similar to that of bulk samples[23], indicating minimal damage due to the FIB fabrication process. In bulk samples of $Gd_3Ru_4Al_{12}$, two long-range magnetic orders exist at zero magnetic field: (1) a proper-screw structure below $T_{N1} = 17.2$ K and (2) sinusoidal magnetic order in the ab plane between $T_{N2} = 18.7$ K and $T_{N1} = 17.2$ K. At both transition temperatures, ρ_{xx}–T shows kinks[23]. Hence, we determined T_{N1} and T_{N2} for our thin-plate samples from kinks in the ρ_{xx}–T curve as shown in Extended Data Fig. 1b. The transition temperatures in the thin-plate samples ($T_{N1} = 16.6$ and $T_{N2} = 17.8$) differ slightly from those in bulk samples. This is probably due to uniaxial strain, which arises from a difference in thermal expansion between the $Gd_3Ru_4Al_{12}$ thin plates and the silicon sample stage.

Determination of magnetic phases for thin-plate devices with H parallel to c-axis

When the magnetic field is applied parallel to the c-axis, $Gd_3Ru_4Al_{12}$ exhibits several magnetic phases: proper-screw, TC, fan, V, skyrmions and induced-ferromagnetic phases[23]. The magnetic structure in phase V is unidentified at the time of writing. We determined these magnetic phases from measurements of magnetoresistivity and Hall conductivity (σ_{xy}) as follows. (1) The TC phase is identified from a dip structure in magnetoresistivity. As shown in Extended Data Fig. 2a–d, ρ_{xx} has a dip structure at low temperatures (blue shading in Extended Data Fig. 2a). In the case of bulk samples, a similar dip structure is observed in the TC phase. Hence, we attribute the observed dip to the formation of the TC structure. (2) The fan-to-ferromagnetic transition is determined from kinks in the H-derivative of magnetoresistivity ($\mathrm{d}\rho_{xx}/\mathrm{d}H$) in the high-field region (green triangles in Extended Data Fig. 2e–h). (3) The skyrmion phase is determined from the topological Hall effect, which appears as an additional contribution to the H-linear normal and M-linear anomalous Hall conductivities. In Extended Data Fig. 2i–l, we present the H-dependence of σ_{xy}. Our field profiles of σ_{xy} exhibit hump-like structures in the intermediate-field region below 10 K (red shading in Extended Data Fig. 2i–k), which we ascribed to the topological Hall contribution due to the formation of skyrmions. Correspondingly, $\mathrm{d}\rho_{xx}/\mathrm{d}H$ also shows kinks at the phase boundaries of the skyrmion phase (red squares in Extended Data Fig. 2e–g). The topological Hall signal gradually emerges from the proper-screw phase, which indicates that the skyrmion phase coexists with other phases such as proper screw and TC phases. This is consistent with the observation of small Im Z^{1f} signal in the skyrmion phase, which is anticipated to originate from the coexisting proper screw and TC phases (see also the main text). (4) We determine the phase boundaries of the V phase from kinks in $\mathrm{d}\rho_{xx}/\mathrm{d}H$ (light blue triangles in Extended Data Fig. 2h). The magnetic phase diagram for the thin-plate samples is similar to that for bulk samples, except for an expansion of the skyrmion phase towards low temperatures. Again, this is probably due to uniaxial strain arising from a difference in thermal expansion.

Frequency dependence of complex impedance measured by lock-in amplifier

In the lock-in measurement, we assume that Im Z^{1f} is governed by the inductive reactance. In addition, since the lock-in measurement is performed below 10 kHz, we ignore the frequency dependence of the inductance, as well as its imaginary part. Both become important above 10 kHz as revealed by LCR measurements. Under these assumptions, the relationship between inductance (L') and the complex impedance can be described as follows:

$$\mathrm{Im}\,\Delta Z^{1f} = \omega L' = 2\pi f L', \quad (5)$$

where $\omega = 2\pi f$ is the angular frequency and Im ΔZ^{1f} is the imaginary part of the background-subtracted complex impedance. We ascribe Im Z^{1f} observed in the paramagnetic phase to the background contribution. To confirm the validity of equation (5), we investigate the frequency dependence of Im ΔZ^{1f}. As shown in Extended Data Fig. 3, Im ΔZ^{1f} increases almost linearly with increasing frequency (f), which indicates that Im Z^{1f} is governed by the inductive reactance.

Emergent inductance for devices of different shapes and electrode materials

We fabricated more than 10 devices to confirm reproducibility and exclude the possibility that the observed signal is due to extrinsic effects, such as external contact contributions. In Extended Data Fig. 4a–e, we show scanning electron microscope images of thin-plate devices with different sizes and geometries. The magnetic-field dependence of the imaginary part of the background-subtracted impedance (Im ΔZ^{1f}) for the corresponding thin-plate devices is shown in Extended Data Fig. 4g–k. Here, the current and frequency were $I = 1$ mA and $f = 10$ kHz, respectively. In all devices, Im ΔZ^{1f} exhibits similar field profiles; Im ΔZ^{1f} is enhanced in the proper-screw helical phase and the TC phase. In addition, as shown in Extended Data Fig. 4m, the magnitude of Im ΔZ^{1f} is proportional to $d_{\mathrm{electrode}}$, indicating that the influence of contacts, if any, is minimal. We also fabricated a device with gold electrodes (Extended Data Fig. 4f); the magnetic-field profile of Im Z^{1f} (Extended Data Fig. 4l) is similar to those for the devices with tungsten electrodes (Extended Data Fig. 4g–k). These results indicate that the observed enhancement of Im Z^{1f} does not originate from an extrinsic factor such as device shape and contact electrodes.

We note that the relative magnitude of Im ΔZ^{1f} in the TC phase with respect to the proper-screw helical phase depends on the device. This is probably due to device-dependent phase coexistence between TC and other competing phases, such as skyrmion and fan. As the transition between TC and the competing orders is a first-order transition, TC can coexist with the other phases. Generally, the ratio of volume fractions for two coexisting phases is sensitive to extrinsic properties such as disorder. Hence, in the present case, probably owing to a slight difference in the number of disorder sites introduced during the device fabrication process, the ratio between TC and the competing phase differs from device to device, which results in device dependence of the magnitude of Im ΔZ^{1f} within the boundaries of TC. In fact, devices with larger Im ΔZ^{1f} in TC show a sharp dip structure in the magnetoresistivity, which is a hallmark of TC as discussed above. In contrast, in the devices with small Im ΔZ^{1f} in TC, the dip structure in magnetoresistivity is smeared out.

Determination of magnetic phases with H parallel to the a-axis

The magnetic phase diagram for thin plates with H // a is determined from measurements of magnetoresistivity and planar Hall resistivity (ρ_{yx}^{PHE}). In Extended Data Fig. 5a, we show H-dependent ρ_{xx} at 5.5 K. There are two kinks in ρ_{xx} (purple and green triangles in Extended Data Fig. 5a). The lowest-field region (green shadow) is a multi-domain proper-screw state with in-plane Q vectors[23]. Since the multi-Q-domain proper-screw is usually transformed to the single-Q conical state with Q // H on increasing the magnetic field, we assign the intermediate phase (light green shading) to the single-Q conical state. The high-field region above 2.5 T is assigned to the ferromagnetic phase.

To confirm this assignment, we measured the planar Hall effect, which can sensitively probe the direction of the Q vector[31]. The relationship between the Q direction and the planar Hall resistivity (ρ_{yx}^{PHE}) can be described as $\rho_{yx}^{\mathrm{PHE}} \propto \sin 2\theta_Q$, where θ_Q is the relative angle between current direction and Q direction. In the single-Q conical state, Q is parallel to the magnetic-field direction, that is, $\theta_Q = \theta_H$ where θ_H is the field angle. Therefore ρ_{yx}^{PHE} is proportional to $\sin 2\theta_H$. In contrast, in the multi-Q-domain proper-screw state, ρ_{yx}^{PHE} does not depend on θ_H because the Q direction does not follow the field direction. In Extended Data Fig. 5b, c, we present the field angle dependence of ρ_{yx}^{PHE}. In the low-field (<0.6 T) phase, ρ_{yx}^{PHE} is independent of θ_H (Extended Data Fig. 5b), consistent with the low-field phase remaining a multi-Q-domain proper-screw phase unaffected by the field direction. In contrast, ρ_{yx}^{PHE} obeys a $\sin 2\theta_H$ dependence in the intermediate-field phase (Extended Data Fig. 5c), indicating that the intermediate-field phase is a single-Q conical state with Q // H. We note that the slight deviation of ρ_{yx}^{PHE} from the $\sin 2\theta_H$ curve is probably due to weak pinning of the Q vector.

Emergent inductance measured with LCR meter

Further experiments were carried out with an LCR meter to check the influence of the electrodes on the frequency dependence of the complex inductance. We thus measured the frequency dependence of the inductance for an additional device with gold electrodes. In Extended Data Fig. 6b, we show the frequency dependence of the complex inductance $\tilde{L}(\omega) = L'(\omega) + iL''(\omega)$ in this device. The observed profile is comparable to that in the device with tungsten electrodes (Fig. 4 in the main text), indicating that the observed frequency dependence, especially suppression of the signal above 10 kHz, does not originate from the influence of contacts.

In Extended Data Fig. 6c–e, we show the magnetic field dependence of Im Z at $f = 7.71$ kHz measured with the LCR meter. Both the magnetic field and current are applied parallel to the a-axis. The magnitude of Im Z is largest at the phase boundary between multi-domain proper-screw and single-domain conical phase and almost zero in the ferromagnetic and paramagnetic phases. These features are all in good agreement with Im Z measured with the lock-in amplifier (Fig. 2k).

Magnitude of the inductance

As shown in the main text, the emergent inductance is approximately −400 nH for a $Gd_3Ru_4Al_{12}$ thin-plate cross-section 0.8 μm^2 and length 9 μm (volume 7.2×10^{-18} m^3). In the case of a commercially used conventional small inductor[32], the inductance is typically 300 nH for a device of size 0.6 mm× 0.3 mm× 0.3 mm (volume 5.4×10^{-11} m^3). Therefore, the inductance value reported here is comparable to that of a commercial inductor, but the volume of the circuit element based on emergent inductance is around 10^6 times smaller.

Data availability

The data that support the findings of this study are available from the corresponding author upon reasonable request.

31. Yokouchi, T. et al. Formation of in-plane skyrmions in epitaxial MnSi thin films as revealed by planar Hall effect. *J. Phys. Soc. Jpn* **84**, 104708 (2015).
32. World's highest inductance values! Expanded lineup of ultra-compact 0201-inch (0603mm)-size high-frequency chip inductors for smartphones — the LQP03TN_02 series-. *muRata* https://article.murata.com/en-eu/article/expanded-lineup-of-ultra-compact-0201-inch-0603mm-size?intcid5 (2014).

Acknowledgements We thank M. Kawasaki for discussions. This work was supported by the Japan Society for the Promotion of Science (JSPS) KAKENHI (grant no. 19K14667) and Core

Research for Evolutional Science and Technology (CREST), Japan Science and Technology Agency (grant no. JPMJCR1874). M.H. was supported as a Humboldt/JSPS International Research Fellow (18F18804).

Author contributions Y.T., N.N. and Y.O. conceived the project. T.Y. fabricated the thin-plate devices and conducted transport measurements with assistance from F.K. M.H. grew and characterized the single crystals. T.Y. and N.N. carried out the theoretical analysis. T.Y., Y.T. and N.N. wrote the draft. All authors discussed the results and commented on the manuscript.

Competing interests The authors declare no competing interests.

Additional information

Supplementary information is available for this paper at https://doi.org/10.1038/s41586-020-2775-x.

Correspondence and requests for materials should be addressed to T.Y. or Y.T.

Peer review information *Nature* thanks Sheonghoon Woo and the other, anonymous, reviewer(s) for their contribution to the peer review of this work.

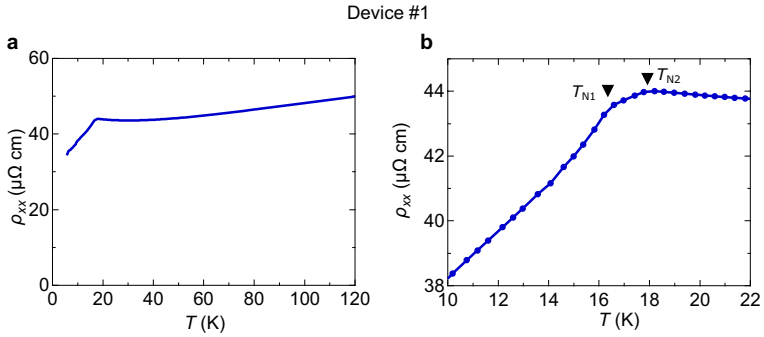

Extended Data Fig. 1 | Temperature dependence of longitudinal resistivity. a, Temperature dependence of resistivity ρ_{xx} for the thin-plate sample of $Gd_3Ru_4Al_{12}$. **b**, Magnified image of ρ_{xx}–T curve around the transition temperature. The transition temperatures (T_{N1} and T_{N2}) are denoted by inverse triangles.

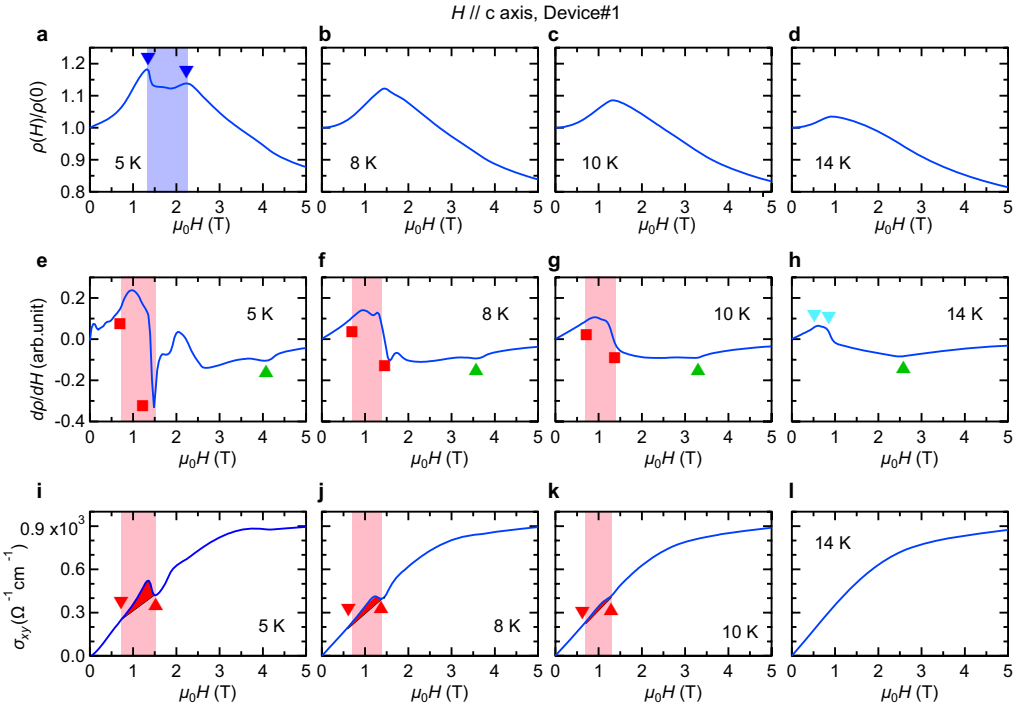

Extended Data Fig. 2 | Magneto-transport properties with *H* // *c*-axis. **a**–**d**, Magnetoresistivity for a thin-plate sample of $Gd_3Ru_4Al_{12}$ at various temperatures. We determined the TC phase from the dip structure represented by the blue shading. **e**–**h**, Magnetic-field derivative of the magnetoresistivity at various temperatures. We ascribe the kinks to the fan-to-ferromagnetic transition (green triangles) and the phase boundaries of the V phase (light blue triangles). The kinks are also observed at the phase boundaries of the skyrmion phase (red squares). **i**–**l**, Magnetic-field dependence of Hall conductivity (σ_{xy}) at various temperatures. The red-shaded regions represent the contribution of the topological Hall effect due to the formation of skyrmions.

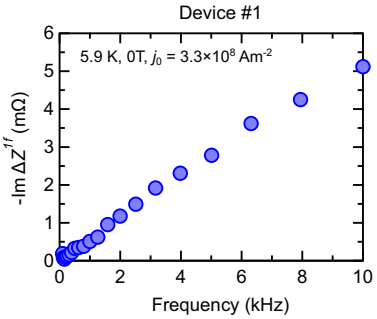

Extended Data Fig. 3 | Frequency dependence of the complex impedance. Frequency dependence of the imaginary part of the background-subtracted complex impedance (Im ΔZ^{1f}), measured with the lock-in amplifier.

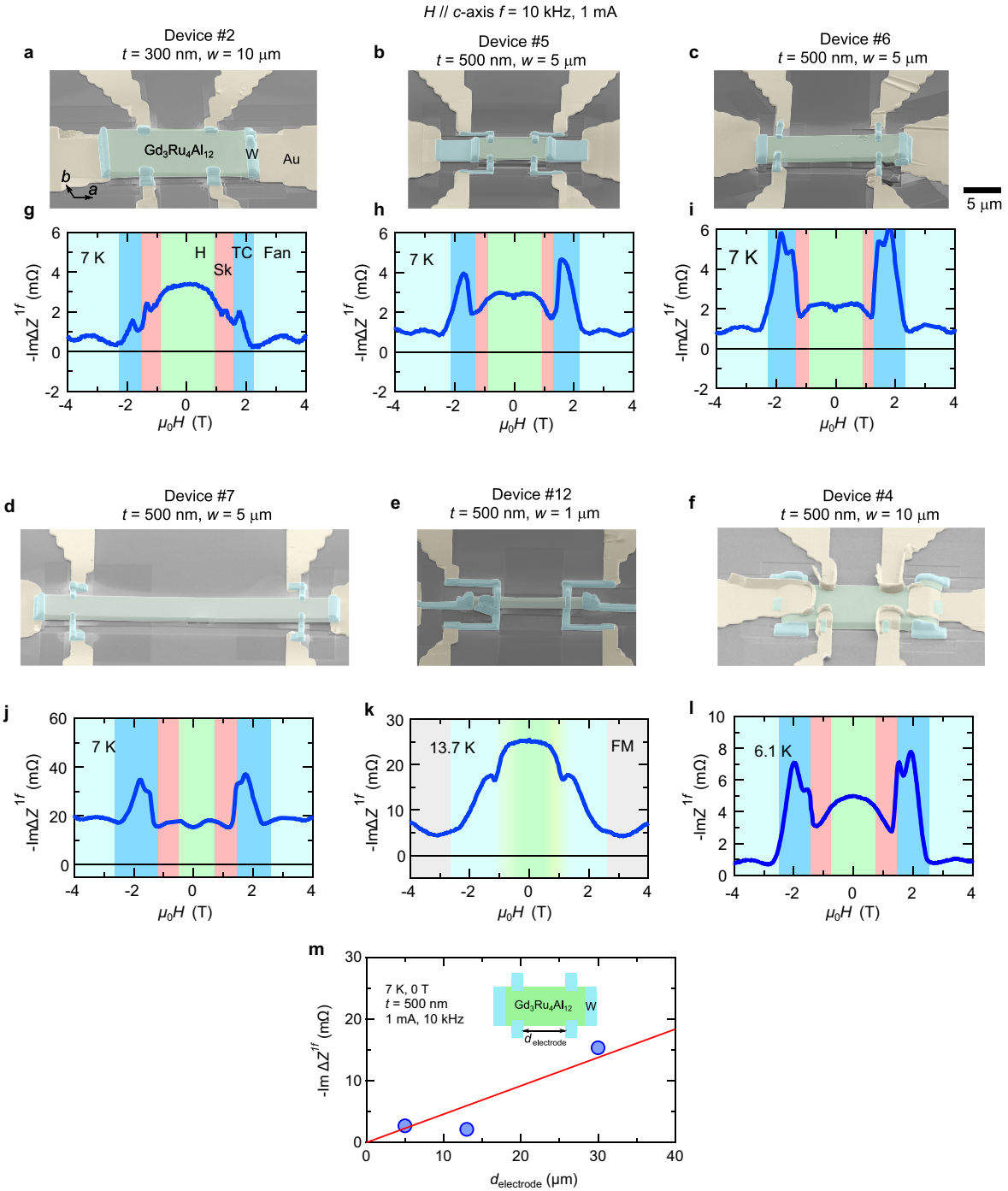

Extended Data Fig. 4 | Emergent inductance for various devices with different size and electrode materials. a–f, Scanning electron microscope images for devices with different sizes and electrode materials. The electrode material is tungsten, except for device 4 in which it is gold. **g–k**, Magnetic-field dependence of the imaginary part of the background-subtracted impedance (Im ΔZ^{1f}) in thin-plate devices with W electrodes. The green, pink, blue and light blue shading represents H, Sk, TC and fan phases, respectively. **l**, Magnetic-field dependence of the imaginary part of the complex impedance Im ΔZ^{1f} in a thin-plate device with gold electrodes. **m**, The magnitude of Im ΔZ^{1f} as a function of the distance of the voltage electrodes ($d_{electrode}$). The definition of $d_{electrode}$ is shown in the inset. Here, the cross-sectional area is the same for all devices shown in **m**.

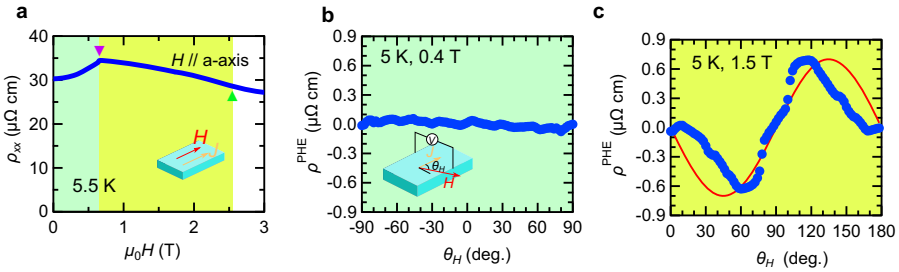

Extended Data Fig. 5 | Magneto-transport properties with *H* parallel to the *a*-axis. a, Magnetoresistivity measured with magnetic field (*H*) and current (*I*) parallel to the *a*-axis at 5.5 K. **b**, **c**, Magnetic-field dependence of planar Hall resistivity (ρ_{yx}^{PHE}) at 0.4 T (**b**) and 1.5 T (**c**). The experimental set-up is shown in the inset in **b**. The red line in **c** is a fit to $\sin 2\theta_H$.

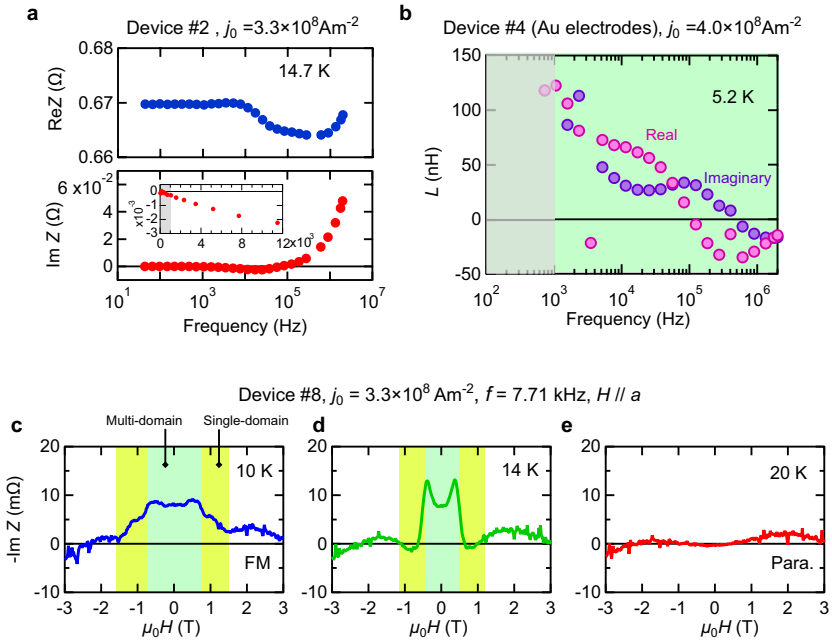

Extended Data Fig. 6 | Emergent inductance measured with LCR meter. **a**, Frequency dependence of complex impedance Z from which we calculated the complex inductance $\tilde{L}(\omega) = L'(\omega) + iL''(\omega)$ (Fig. 4b). The inset is the magnified view of Im Z in the low-frequency range on a linear scale. Grey shading corresponds to the grey-shaded region in Fig. 4b. **b**, Frequency dependence of $\tilde{L}(\omega)$ for a thin-plate device with gold electrodes. **c**–**e**, Magnetic field dependence of the imaginary part of the complex impedance (Im Z) measured with an LCR meter at various temperatures, for magnetic field applied in the hexagonal plane. See Methods for the procedure for extracting the bulk contribution of Z.